GRAIN BOUNDARY MIGRATION WITH THERMAL GROOVING EFFECTS: A NUMERICAL APPROACH

VADIM DERKACH, AMY NOVICK-COHEN, AND ARKADY VILENKIN

Abstract. Grain boundary migration in the presence of thermal grooving effects play a critical role in the stability of the thin polycrystalline films used in numerous technological applications. We present a computational framework for simulating this motion which relies on a physical model due to Mullins [33, 26], according to which the grain boundaries and the external surfaces are governed by mean curvature motion and surface diffusion, respectively, and along the thermal grooves where the grain boundaries and the exterior surfaces couple, balance of mechanical forces, continuity of the chemical potential, and balance of mass flux dictate the boundary conditions. By adopting an equi-spaced parametric description for the evolving surfaces [40, 13], the physical model can be formulated as a coupled systems of ODEs and PDEs.

We propose a finite difference algorithm based on staggered grids for solving the resultant system, which we implement on a polycrystalline layer with columnar structure containing three grains, assuming isotropy. Our algorithm, which is second order accurate in space and first order accurate in time, conserves mass, dissipates energy, and satisfies the predictions of Mullins[33], von Neumann-Mullins [32, 51] and Génin, Mullins, Wynblatt [22], in appropriate limits. Effects such as pitting, hole formation, grain annihilation, wetting, and dewetting can be analyzed using our approach [15, 14, 17, 16].

1. INTRODUCTION

We report on a numerical algorithm designed to study simultaneous grain boundary migration and surface topography evolution in polycrystalline films with columnar structure, which is particularly relevant for studying thin polycrystalline films. Simultaneous grain boundary migration and surface topography evolution often strongly affect the thermal stability of thin polycrystalline films, which are of high technological importance, since at temperatures which enable some surface diffusion, grooves form on the exterior surface where grain boundaries emerge, and these grooves can penetrate down to the substrate, leading to hole formation and sometimes eventually to full agglomeration [48].

Over recent years, there has been a plentitude of studies devoted to modeling microstructural evolution in polycrystalline materials, taking into account a large spectrum of effects. The majority have focused on the microstructural evolution within the interior of the specimen, with recent emphasis on their statistical properties [32, 23, 44, 5, 4, 49]. Microstructural evolution of the exterior surface topology has also been studied, though to a lesser extent; there have been studies focusing on facetting, anisotropy, and stability, with some emphasis on grooving, traveling wave solutions, stagnation, and self-similarity [34, 22, 11, 28, 1, 42]. The number of studies focusing on the coupled motion of the two effects is markedly less abundant. While the analytic framework for the coupled motion has yet to become fully developed, numerical methods have been proposed and implemented, certain bicrystalline geometries, with special initial and boundaries conditions, have been treated in depth, and various phenomena, such as grooving, migration, and pitting, have received attention [34, 50, 26, 28, 38, 31, 52]. Recent experiments have reported on the possibility of accompanying phenomena such as mazing [43], which for simplicity we do not attempt to model.

In the present paper we outline and test an algorithm which was developed to follow the evolution of coupled surface and grain boundary phenomena in realistic polycrystalline microstructures. In earlier papers, we used this algorithm to describe simultaneous grain boundary migration and grooving in a triangular bamboo three grain geometry in a thin polycrystalline specimen, which can exhibit hole formation and grain annihilation [15] as well as stabilization of hexagonal arrays [17]. Here, we present a detailed discussion of our numerical algorithm, which is based on a parametric description of the evolving surfaces, with equidistributed grid points on a staggered grid. Our approach generalizes the primarily 2D algorithm proposed by Pan and Wetton [40, 39, 10, 41]. Numerical methods, such as level set methods, thresholding dynamics, and MBO methods [45, 3, 19, 29], which have been widely utilized in simulating microstructural evolution, are not directly applicable for the coupled motions considered here. Potentially phase field methods based on [37], could be implemented here, but this is also not straightforward. While finite element algorithms have been proposed and analysed, and could be potentially useful for geometries such as we consider [47, 8, 7, 6]; however realistic multi-grain geometries in R^3 governed by the coupled motions have so far received only very limited attention.

The outline of the paper is as follows. In Section 2, we present the physical model, the geometry to be considered, and the governing laws of motion. In Section 3, we explain the parametric descriptions with equi-spacing which we adopt to describe the various evolving surfaces, and outline the resultant parametric problem formulation. Section 4 contains a detailed account of our algorithm. Section 5 provides some results pertaining to pitting and grain annihilation, energy dissipation and mass conservation. Our results are compared with the small slope approximation predictions of von Neumann-Mullins [32, 51], Mullins [33], and Génin, Mullins, Wynblatt [22]. Conclusions are given in Section 6.

2. The physical model: geometry and laws of motion

We focus on an idealized three grain system, which can be extended by reflection to yield a five grain system, see Fig. 1. The grains in the system are assumed to be of the same material, but to have different crystalline lattice orientations. For simplicity, we assume isotropy and neglect the possible effects of elasticity, evaporation, defects, and volume diffusion. Our three grain system contains three grain boundaries, three exterior surfaces and five bounding
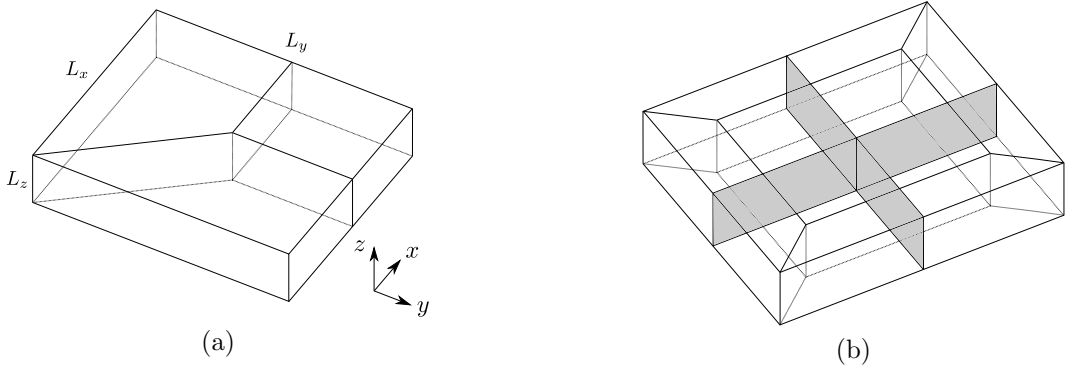
FIGURE 1. Sketch of (a) the three grain system, and (b) the resultant five grain system geometry.

planes. The three grain boundaries are assumed to evolve by mean curvature motion [32, 33],

$$(2.1) \qquad V_n = \mathcal{A} H,$$

and the three exterior surfaces are assumed to evolve by surface diffusion motion [33, 34],

$$(2.2) \qquad V_n = -\mathcal{B} \triangle_s H.$$

In (2.1)–(2.2), V_n denotes the normal velocity of the evolving surface, H denotes its mean curvature, and $\triangle_s$ is the Laplace–Beltrami operator, known also as the "surface Laplacian." In (2.1), $\mathcal{A}$ is a kinetic coefficient known as the reduced mobility, and in (2.2), $\mathcal{B}$ is a kinetic coefficient known as the surface diffusion coefficient. Mirror symmetry is assumed with respect to the five bounding planes, which are assumed to be stationary.

Boundary conditions need to be prescribed where an evolving surface intersects another evolving surface or a bounding plane. The intersection of a grain boundary with two exterior surfaces defines a "triple junction line," known also as a "thermal groove" or a "groove root," and the intersection of three grain boundaries will be referred to as an "internal triple junction line." The intersection of a grain boundary or an exterior surface with a bounding plane will be referred to as an "exterior free boundary." The intersection of three groove roots with an internal triple junction line defines a "quadruple point," and the intersections of two exterior free boundaries define "corner points."

Along groove roots, we impose i) "persistence;" namely that the grain boundary and the exterior surfaces remain attached, ii) balance of mechanical forces known also as Young's law, which is an isotropic version of Herring's law [24, 25], namely that

$$(2.3) \qquad \vec{\tau}^i \cdot \vec{\tau}^j = \cos(\theta), \quad \vec{\tau}^i \cdot \vec{\tau}^k = \vec{\tau}^j \cdot \vec{\tau}^k = -\cos(\theta/2),$$

where $\vec{\tau}^i$, $\vec{\tau}^j$, and $\vec{\tau}^k$ are orthogonal to the groove root and correspond to the unit tangents to two exterior surfaces and to a grain boundary surface, respectively, which intersect along the groove root, and θ, the "dihedral angle," is defined as

$$(2.4) \qquad \theta = \pi - 2 \arcsin(m/2), \quad m = \gamma_{gb}/\gamma_{ext},$$

where γ_{gb} and γ_{ext} are the energy/area of the grain boundary and of the exterior surfaces, respectively. iii) continuity of the chemical potential, and iv) balance of mass flux. We shall

be assuming that the chemical potential is proportional to the mean curvature and that mass flux is proportional to the gradient of the chemical potential, see [34, 26, 27]. Along the internal triple junction line, which we shall assume to be unique we impose "persistence" as well as

$$(2.5) \qquad \vec{\tau}^i \cdot \vec{\tau}^j = \cos(2\pi/3),$$

where $\vec{\tau}^i$, $\vec{\tau}^j$ are unit vectors which are orthogonal to the internal triple junction line and which are tangent to one of the two intersecting grain boundary surfaces. We refer also to (2.5) as Young's law, since taking $m = 1$ in (2.4) because the energy/area of the various grain boundaries are equal, we obtain that $2\pi/3 = \pi - 2\arcsin(1/2)$; then $\cos(2\pi/3) = -\cos(\pi/3)$, so that (2.3) is satisfied

Along the exterior free boundaries, where an exterior surface intersects a bounding plane, we impose "persistence," mirror symmetry, and zero mass flux. Along the free boundaries where a grain boundary intersects a bounding plane, we impose a "persistence" and mirror symmetry. The boundary conditions at the quadruple junction and the corner points will be described in detail in Section 3.5. Initial conditions are prescribed in accordance with Fig. 2.

Since (2.1)–(2.2) prescribe only the normal velocities of the surfaces, the governing equations may be formulated as an evolutionary problem via various equivalent descriptions [21]. We adopt an approach based on equi-spaced parametric representations of the various surfaces, which yield equi-distributed grid points when solved using finite differences and ghost points. While alternatively we might prescribe the tangential velocities, at least in R^2 equi-distribution of the grid points was noted to have an overall stabilizing effect on the resultant algorithms [40, 9]. Our method generalizes the methodology proposed by Pan & Wetton [40, 39], which was implemented primarily for simple geometries in R^2, and was influenced also by earlier works such as [3].

3. THE PARAMETRIC PROBLEM FORMULATION

3.1. **Parametric representations with equi-spacing.** The evolving surfaces, which we denote by S^i, $i \in \{1, \ldots, 6\}$, will be assumed to be representable by parametric hypersurfaces, $X^i : [0,1]^2 \times [0,T] \to R^3$, namely

$$(3.1) \qquad X^i(\alpha, \beta, t) = \left(x^i(\alpha, \beta, t), y^i(\alpha, \beta, t), z^i(\alpha, \beta, t)\right), \quad 0 \le \alpha, \beta \le 1, \quad 0 \le t \le T,$$

for some $T > 0$, where the Cartesian coordinates (x, y, z) are indicated in Fig. 1. Rather than specifying somewhat arbitrary tangential velocities, we impose equi-spacing of the (α, β) parametrization, namely that $\|X_\alpha\|_\alpha = \|X_\beta\|_\beta = 0$, which implies that

$$(3.2) \qquad \langle X_\alpha, X_{\alpha\alpha} \rangle = \langle X_\beta, X_{\beta\beta} \rangle = 0,$$

where X represents one of the six surfaces, X^i. We shall be implicitly assuming sufficiently regular and non-degeneracy, $\|X_\alpha\|, \|X_\beta\| > 0$, of the surfaces X^i up to some time T.

The orientation of parameterizations for the various surfaces are indicated in Fig. 2, where S^i, $i \in \Psi_{ext} := \{1, 2, 3\}$, refer to exterior surfaces and S^i, $i \in \Psi_{gb} := \{4, 5, 6\}$, refer to grain boundaries. The vectors $\vec{\tau}^{i\alpha}$, $\vec{\tau}^{i\beta}$ denote tangent vectors to the surface S^i, are given in (3.6) and (3.7), respectively, and satisfy $\vec{\tau}^{i\alpha} \perp X_\alpha^i$ and $\vec{\tau}^{i\beta} \perp X_\beta^i$. From Fig 2, one can see the 3 triple junction lines where two exterior surfaces, S^p, S^q, intersect with the grain boundary surface S^ℓ, for $\{p, q, \ell\} \in \Psi_{thermal} := \{\{1, 2, 4\}; \{2, 3, 5\}; \{3, 1, 6\}\};$
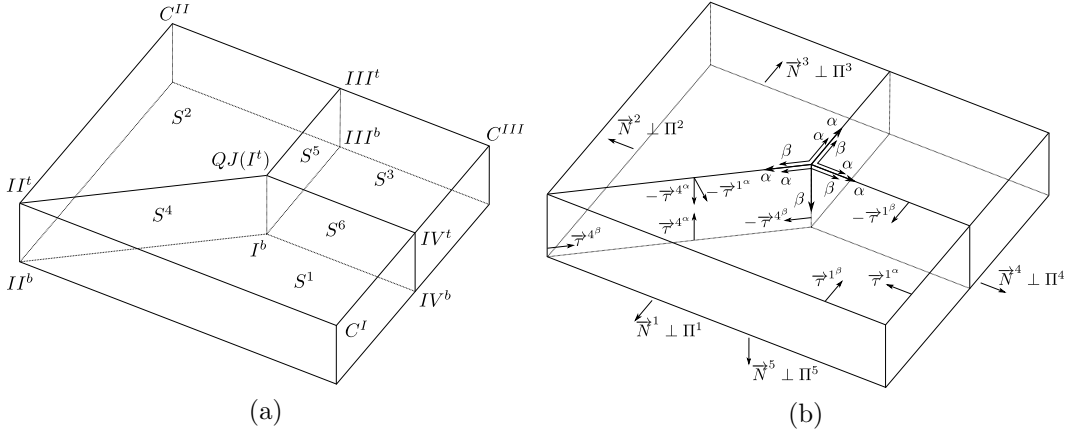
FIGURE 2. The system of 3 grains. The exterior surfaces, S^i, $i \in \Psi_{ext} :=$ $\{1, 2, 3\}$ as well as the grain boundary surfaces, S^i, $i \in \Psi_{gb} := \{4, 5, 6\}$ are indicated in (a), as are the bounding planes II^i, $i = 1, \ldots, 5$, and the respective unit normals to these bounding planes, $\vec{N}^i$, $i = 1, \ldots, 5$. The quadruple junction (QJ) is indicated as I^t, and $\Psi_{corner} := \{II^t, III^t, IV^t, I^b, II^b, III^b, IV^b, C^I, C^{II}, C^{III}\}$ refer to the remaining corner points. In (b), on each surface S^i, $i \in \Psi_{ext} \cup \Psi_{gb}$, the orientation of the α–β parameterization is indicated, as are the various tangents to these surfaces, $\vec{\tau}^{i^\alpha}$, $\vec{\tau}^{i^\beta}$, $i = 1, \ldots, 6$; here $\vec{\tau}^{i^\alpha}$ and $\vec{\tau}^{i^\beta}$ correspond to the tangents to S^i in the direction of the α–parameterization and the β-parameterization, respectively, see text.

along these triple junction lines, thermal grooves will form in our system when $m > 0$. There is also one internal triple junction line where the 3 grain boundary surfaces S^4, S^5, S^6 intersect. Moreover, there are 5 bounding planes of symmetry, indicated by Π^i, $i = 1, \ldots 5$ in Fig 2, where Π^5 refers to the "midplane" or base plane of the system located at $z = 0$; the unit normal vectors $\vec{N}^i$ to Π^i are also indicated. In Fig 2, the location of the quadruple junction (QJ) is indicated by I^t, and the other corner points $\Psi_{I,C} := \{II^t, III^t, IV^t, I^b, II^b, III^b, IV^b, C^I, C^{II}, C^{III}\}$ are also indicated.

3.2. **Equations governing the grain boundaries and exterior surfaces.** In order to express (2.1)–(2.2) in terms of the parametric surfaces, X^i, let S denote one of the evolving surfaces whose parametrization is given by X. Then its normal velocity can be expressed as

$$(3.3) \qquad \vec{V_n} = \langle X_t, \vec{n} \rangle.$$

where $\vec{n} = \frac{X_\alpha \times X_\beta}{\|X_\alpha \times X_\beta\|}$ is a unit normal to S. Its mean curvature H can be expressed as [20]

$$(3.4) \qquad H = \frac{1}{2} \left\langle \frac{\langle X_\beta, X_\beta \rangle X_{\alpha\alpha} - 2 \langle X_\alpha, X_\beta \rangle X_{\alpha\beta} + \langle X_\alpha, X_\alpha \rangle X_{\beta\beta}}{\langle X_\alpha, X_\alpha \rangle \langle X_\beta, X_\beta \rangle - \langle X_\alpha, X_\beta \rangle^2}, \vec{n} \right\rangle,$$

The Laplace–Beltrami operator $\triangle_s$ may be defined as $\triangle_s = \nabla_s \cdot \nabla_s$ where $\nabla_s = \nabla - \vec{n} \, \partial_{\vec{n}}$, [20]. If $P(\alpha, \beta)$ is a smooth field is defined on the parametric surface $X = X(\alpha, \beta)$,

then (see [20])

$$\nabla_s P = \frac{\langle X_\beta, X_\beta \rangle \, X_\alpha - \langle X_\alpha, X_\beta \rangle \, X_\beta}{\langle X_\alpha, X_\alpha \rangle \, \langle X_\beta, X_\beta \rangle - \langle X_\alpha, X_\beta \rangle^2} \, P_\alpha + \frac{\langle X_\alpha, X_\alpha \rangle \, X_\beta - \langle X_\alpha, X_\beta \rangle \, X_\alpha}{\langle X_\alpha, X_\alpha \rangle \, \langle X_\beta, X_\beta \rangle - \langle X_\alpha, X_\beta \rangle^2} \, P_\beta,$$

and straightforward technical calculations yield that

(3.5)
$$\triangle_s H = \frac{\langle X_\beta, X_\beta \rangle \, H_{\alpha\alpha} - 2 \, \langle X_\alpha, X_\beta \rangle \, H_{\alpha\beta} + \langle X_\alpha, X_\alpha \rangle \, H_{\beta\beta}}{\langle X_\alpha, X_\alpha \rangle \, \langle X_\beta, X_\beta \rangle - \langle X_\alpha, X_\beta \rangle^2} +$$

$$\frac{\left\langle \langle X_\alpha, X_\alpha \rangle \, X_{\beta\beta} - 2 \, \langle X_\alpha, X_\beta \rangle \, X_{\alpha\beta} + \langle X_\beta, X_\beta \rangle \, X_{\alpha\alpha}, |\langle X_\beta, X_\beta \rangle|^{1/2} \overrightarrow{\tau}^\beta \right\rangle}{\left(\langle X_\alpha, X_\alpha \rangle \, \langle X_\beta, X_\beta \rangle - \langle X_\alpha, X_\beta \rangle^2 \right)^{3/2}} \, H_\alpha +$$

$$\frac{\left\langle \langle X_\alpha, X_\alpha \rangle \, X_{\beta\beta} - 2 \, \langle X_\alpha, X_\beta \rangle \, X_{\alpha\beta} + \langle X_\beta, X_\beta \rangle \, X_{\alpha\alpha}, |\langle X_\alpha, X_\alpha \rangle|^{1/2} \overrightarrow{\tau}^\alpha \right\rangle}{\left(\langle X_\alpha, X_\alpha \rangle \, \langle X_\beta, X_\beta \rangle - \langle X_\alpha, X_\beta \rangle^2 \right)^{3/2}} \, H_\beta,$$

where

(3.6)
$$\overrightarrow{\tau}^\alpha = \frac{X_\alpha \, \langle X_\alpha, X_\beta \rangle - X_\beta \, \langle X_\alpha, X_\alpha \rangle}{|\langle X_\alpha, X_\alpha \rangle|^{1/2} \cdot |\langle X_\alpha, X_\alpha \rangle \, \langle X_\beta, X_\beta \rangle - \langle X_\alpha, X_\beta \rangle^2|^{1/2}},$$

(3.7)
$$\overrightarrow{\tau}^\beta = \frac{X_\beta \, \langle X_\alpha, X_\beta \rangle - X_\alpha \, \langle X_\beta, X_\beta \rangle}{|\langle X_\beta, X_\beta \rangle|^{1/2} \cdot |\langle X_\alpha, X_\alpha \rangle \, \langle X_\beta, X_\beta \rangle - \langle X_\alpha, X_\beta \rangle^2|^{1/2}}.$$

Since the exterior surfaces S^i, $i \in \Psi_{ext}$ evolve by surface diffusion (2.2) and the grain boundaries S^i, $i \in \Psi_{gb}$ evolve by mean curvature motion (2.1), we get that

(3.8)
$$\langle X_t^i, \overrightarrow{n}^i \rangle = -\triangle_s H^i, \quad i \in \Psi_{ext} := \{1, 2, 3\},$$

(3.9)
$$\langle X_t^i, \overrightarrow{n}^i \rangle = H^i, \quad i \in \Psi_{gb} := \{4, 5, 6\},$$

where explicit expressions for $\overrightarrow{n}$, H, and $\triangle_s H$ were prescribed in (3.4)–(3.5).

3.3. **Conditions along triple junctions lines.** As noted our system contains three thermal grooves where two exterior surfaces, S^p, S^q, intersect a grain boundary S^ℓ, for $\{p, q, \ell\} \in \Psi_{thermal} := \{\{1, 2, 4\}; \{2, 3, 5\}; \{3, 1, 6\}\}$. From Fig 2, we see that each thermal groove possesses natural parametrizations with respect to α along S^p and S^ℓ and with respect to β along S^q. Recalling that the conditions to be imposed include persistence, Young's law, continuity of the chemical potential, continuity of mass flux as well as equi-spacing of the parametrization, we obtain that

(3.10)
$$X^p = X^q = X^\ell, \quad \text{(persistence)}$$

(3.11)
$$\left\langle \overrightarrow{\tau}^{\ell\alpha}, \overrightarrow{\tau}^{p\alpha} \right\rangle = \left\langle \overrightarrow{\tau}^{\ell\alpha}, \overrightarrow{\tau}^{q\beta} \right\rangle = \cos(\pi - \theta/2), \quad \text{(Young's law)}$$

(3.12)
$$\langle X_\alpha^p, X_{\alpha\alpha}^p \rangle = 0, \quad \text{(equi-spacing)}$$

(3.13)
$$H^p = H^q, \quad \text{(continuity)}$$

(3.14)
$$\left\langle \nabla_s H^1, \overrightarrow{\tau}^{p\alpha} \right\rangle + \left\langle \nabla_s H^q, \overrightarrow{\tau}^{q\beta} \right\rangle = 0, \quad \text{(balance of mass flux)},$$

where θ is the dihedral angle, see (2.4). Expressions for H, $\nabla_s H$, $\overrightarrow{\tau}^\alpha$, $\overrightarrow{\tau}^\beta$ were given in (3.4)-(3.7).

Along the internal triple junction line, where the grain boundaries S^4, S^5, S^6 intersect, there is a natural parametrization with respect to β. Here persistence, Young's law, and equi-spacing imply that

$$X^4 = X^5 = X^6, \qquad \text{(persistence)} \tag{3.15}$$

$$\left\langle \vec{\tau}^{4\beta}, \vec{\tau}^{5\beta} \right\rangle = \left\langle \vec{\tau}^{4\beta}, \vec{\tau}^{6\beta} \right\rangle = \cos\left(2\pi/3\right), \qquad \text{(Young's law)} \tag{3.16}$$

$$\left\langle X^4_\beta, X^4_{\beta\beta} \right\rangle = 0, \qquad \text{(equi-spacing)}. \tag{3.17}$$

3.4. Conditions along the exterior free boundaries.
Along the intersections of the exterior surface S^p with the bounding planes Π^q and Π^ℓ, for $\{p, q, \ell\} \in \Psi_{fb}$ where $\Psi_{fb} := \left\{\{1, 4, 1\}; \{2, 2, 3\}; \{3, 3, 4\}\right\}$, we impose the conditions

$$\left\langle X^p - r^q_0, \vec{N}^q \right\rangle = \left\langle X^p - r^\ell_0, \vec{N}^\ell \right\rangle = 0, \qquad \text{(attachment)} \tag{3.18}$$

$$\left\langle \vec{n}^p, \vec{N}^q \right\rangle = \left\langle \vec{n}^p, \vec{N}^\ell \right\rangle = 0, \qquad \text{(symmetry)} \tag{3.19}$$

$$\left\langle X^p_\alpha, X^p_{\alpha\alpha} \right\rangle = \left\langle X^p_\beta, X^p_{\beta\beta} \right\rangle = 0, \qquad \text{(equi-spacing)} \tag{3.20}$$

$$\left\langle \nabla_s H^p, \vec{N}^q \right\rangle = \left\langle \nabla_s H^p, \vec{N}^\ell \right\rangle = 0, \qquad \text{(zero mass flux)}. \tag{3.21}$$

Note that

$$\left\langle r - r^i_0, \vec{N}^i \right\rangle = 0, \tag{3.22}$$

prescribes the bounding planes Π^i, $i = 1, \ldots 5$, where $\vec{N}^i$ is a unit normal vector to Π^i and r^i_0 is a point on Π^i, which in our numerics will be chosen to be bounded away from the evolving surfaces.

Along the intersection of grain boundary S^p, for $p = \Psi_{gb}$, with Π^5, we impose

$$\left\langle X^p - r^5_0, \vec{N}^5 \right\rangle = 0, \qquad \text{(attachment)} \tag{3.23}$$

$$\left\langle \vec{n}^p, \vec{N}^5 \right\rangle = 0, \qquad \text{(symmetry)} \tag{3.24}$$

$$\left\langle X^p_\alpha, X^p_{\alpha\alpha} \right\rangle = 0, \qquad \text{(equi-spacing)}. \tag{3.25}$$

Similarly along the intersections of S^4 with Π^1 and Π^2, we set

$$\left\langle X^4 - r^1_0, \vec{N}^1 \right\rangle = \left\langle X^4 - r^2_0, \vec{N}^2 \right\rangle = 0, \qquad \text{(attachment)} \tag{3.26}$$

$$\left\langle \vec{n}^4, \vec{N}^1 \right\rangle = \left\langle \vec{n}^4, \vec{N}^2 \right\rangle = 0, \qquad \text{(symmetry)} \tag{3.27}$$

$$\left\langle X^4_\beta, X^4_{\beta\beta} \right\rangle = 0, \qquad \text{(equi-spacing)}. \tag{3.28}$$

and along the intersections of S^p with Π^ℓ for $\{p, \ell\} \in \left\{\{5, 3\}; \{6, 4\}\right\}$,

$$\left\langle X^p - r^\ell_0, \vec{N}^\ell \right\rangle = 0, \qquad \text{(attachment)} \tag{3.29}$$

$$\left\langle \vec{n}^p, \vec{N}^\ell \right\rangle = 0, \qquad \text{(symmetry)} \tag{3.30}$$

$$\left\langle X^p_\beta, X^p_{\beta\beta} \right\rangle = 0, \qquad \text{(equi-spacing)}. \tag{3.31}$$

Although the conditions of the form $\left\langle \overrightarrow{n}, \overrightarrow{N} \right\rangle = 0$ could have been replaced by conditions of the form $\left\langle \overrightarrow{\tau}, \overrightarrow{N} \right\rangle = 1$, the former turned out to be easier to handle numerically.

3.5. **Conditions at the quadruple junction and at the corner points.** In this subsection, we describe the conditions imposed at the quadruple junction and at the other corner points, $\Psi_{I\,C} := \left\{ I^t, II^t, III^t, IV^t, I^b, II^b, III^b, IV^b, C^I, C^{II}, C^{III} \right\}$, see in Fig 2. The balance of mass flux conditions will be discussed in detail in Section 3.6.

Conditions at I^t, the quadruple junction (QJ). At I^t we set

(3.32) $$X^1 = X^2 = X^3 = X^4 = X^5 = X^6, \qquad \text{(persistence)}$$

(3.33) $$\left\langle \frac{X^4_\beta}{\|X^4_\beta\|}, \frac{X^j_\alpha}{\|X^j_\alpha\|} \right\rangle = \cos(\phi), \ j = 1, 2, 3, \qquad \text{(angle condition)}$$

(3.34) $$H^1 = H^2 = H^3, \qquad \text{(continuity)}$$

(3.35) $$\sum_{i=1}^3 \int_{\Gamma^i} \overrightarrow{n}^{\Gamma^i} \cdot \nabla_s H^i \, ds_i = 0, \qquad \text{(balance of mass flux)}.$$

The angle condition at the quadruple junction follows from assuming that the angle conditions prescribed by Young's law hold smoothly up to the quadruple junction; this in particular implies that $\cos(\phi) = -\frac{1}{\sqrt{3}} \frac{m}{\sqrt{4-m^2}}$, see [14]. The curve Γ^i which appears above as well as in the balance of mass flux conditions which follow, corresponds to a smooth curve which normally intersects the bounding thermal grooves, see Section 3.6, and s^i corresponds to an arc-length parametrization of Γ^i.

Conditions at I^b. At I^b, where S^4, S^5, S^6 and Π^5 meet, we set

(3.36) $$X^4 = X^5 = X^6 \qquad \text{(persistence)}$$

(3.37) $$\left\langle X^4 - r^5_0, \overrightarrow{N}^5 \right\rangle = 0, \qquad \text{(attachment)}$$

(3.38) $$\left\langle \frac{X^4_\alpha}{\|X^4_\alpha\|}, \frac{X^5_\alpha}{\|X^5_\alpha\|} \right\rangle = \left\langle \frac{X^4_\alpha}{\|X^4_\alpha\|}, \frac{X^6_\alpha}{\|X^6_\alpha\|} \right\rangle = \cos\left(\frac{2}{3}\pi\right), \qquad \text{(Young's law)}.$$

Conditions at II^b. The point II^b, where S^4, Π^1, Π^2, and Π^5 meet, is stationary, hence

(3.39) $$\left\langle X^4 - r^1_0, \overrightarrow{N}^1 \right\rangle = \left\langle X^4 - r^2_0, \overrightarrow{N}^2 \right\rangle = \left\langle X^4 - r^5_0, \overrightarrow{N}^5 \right\rangle = 0, \quad \text{(attachment)}.$$

Conditions at III^b and IV^b. At III^b, where S^5, Π^3, Π^5, intersect, we impose

(3.40) $$\left\langle \overrightarrow{n}^5, \overrightarrow{N}^3 + \overrightarrow{N}^5 \right\rangle = 0, \qquad \text{(symmetry)}$$

(3.41) $$\left\langle X^5 - r^3_0, N^3 \right\rangle = \left\langle X^5 - r^5_0, \overrightarrow{N}^5 \right\rangle = 0. \qquad \text{(attachment)}.$$

We should have liked to require that $\left\langle \overrightarrow{n}^5, \overrightarrow{N}^3 \right\rangle = \left\langle \overrightarrow{n}^5, \overrightarrow{N}^5 \right\rangle = 0$; however looking at the conditions imposed along the intersection of S^p with Π^5 for $p = \Psi_{gb}$, and along the

intersections of S^p with Π^ℓ for $\{p, \ell\} \in \left\{ \{5, 3\}; \{6, 4\} \right\}$, this appears to be overly restrictive. The conditions at IV^b are analogous.

Conditions at II^t. At II^t, where S^1, S^2, S^4 and Π^1, Π^2 intersect, we impose

$$(3.42) \qquad X^1 = X^2 = X^4, \qquad \text{(persistence)}$$

$$(3.43) \qquad \left\langle \frac{X^4_\alpha}{\|X^4_\alpha\|}, \overrightarrow{N}^1 \times \overrightarrow{N}^2 \right\rangle = 0, \qquad \text{(symmetry)}$$

$$(3.44) \qquad \left\langle X^4 - r^1_0, \overrightarrow{N}^1 \right\rangle = \left\langle X^4 - r^2_0, \overrightarrow{N}^2 \right\rangle = 0, \qquad \text{(attachment)}$$

$$(3.45) \qquad H^1 = H^2, \qquad \text{(continuity)}$$

$$(3.46) \qquad \sum_{i=1}^{2} \int_{\Gamma^i} \overrightarrow{n}^{\Gamma^i} \cdot \nabla_s H^i \, ds_i = 0, \qquad \text{(balance of mass flux)}.$$

Condition (3.43) constitutes a seemingly "minimal" mirror symmetry condition.

Conditions at C^I, C^{II} and C^{III}. At C^I, where S^1, Π^1, and Π^4 intersect, we set

$$(3.47) \qquad \left\langle \overrightarrow{n}^1, \overrightarrow{N}^1 + \overrightarrow{N}^4 \right\rangle = 0, \qquad \text{(symmetry)}$$

$$(3.48) \qquad \left\langle X^1 - r^1_0, \overrightarrow{N}^1 \right\rangle = \left\langle X^1 - r^4_0, \overrightarrow{N}^4 \right\rangle = 0, \qquad \text{(attachment)}$$

$$(3.49) \qquad \int_{\Gamma^1} \overrightarrow{n}^{\Gamma^1} \cdot \nabla_s H^1 \, ds_1 = 0, \qquad \text{(zero mass flux)}$$

where (3.47) has been prescribed in analogy with (3.40). At C^{II} and at C^{III}, where S^2, Π^2, Π^3, and S^3, Π^3, Π^4, respectively, intersect, analogous conditions are prescribed.

Conditions at III^t and IV^t. At III^t where S^2, S^3, S^5 and Π^3 intersect, we set

$$(3.50) \qquad X^2 = X^3 = X^5, \qquad \text{(persistence)}$$

$$(3.51) \qquad \left\langle \overrightarrow{n}^5, \overrightarrow{N}^3 \right\rangle = \left\langle X^5_\alpha, X^5_\beta \right\rangle = 0, \qquad \text{(symmetry)}$$

$$(3.52) \qquad \left\langle X^5 - r^3_0, \overrightarrow{N}^3 \right\rangle = 0, \qquad \text{(attachment)}$$

$$(3.53) \qquad H^2 = H^3, \qquad \text{(continuity)}$$

$$(3.54) \qquad \sum_{i \in \{2,3\}} \int_{\Gamma^i} \overrightarrow{n}^{\Gamma^i} \cdot \nabla_s H^i \, ds_i = 0. \qquad \text{(balance of mass flux)}$$

At IV^t, where S^1, S^3, S^6 and Π^4 intersect, analogous conditions are imposed.

3.6. Approximation of the integral in the mass flux conditions. In Section 3.5, balance of mass flux at the quadruple junction and at the top corner points was prescribed in terms of a condition which included integrals of the form

$$(3.55) \qquad \int_{\Gamma} \overrightarrow{n}^{\Gamma} \cdot \nabla_s H \, ds,$$

where Γ is a curve lying on the exterior surface S which is bounded on either end by bounding planes or by thermal grooves. We now prescribe more precisely the curve Γ, as well as our
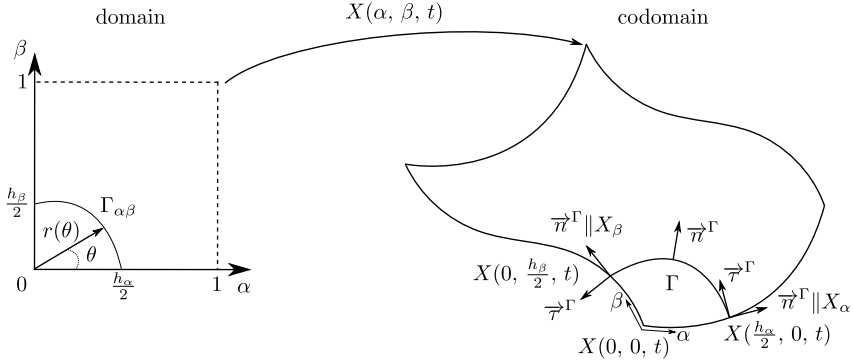

FIGURE 3. A sketch of relationship between $\Gamma_{\alpha\beta}$, Γ and $X(\alpha, \beta, t)$.

approximation of the integral (3.55), near the point $X(0, 0, t)$. See Fig. 3. The treatment at the other corner points is analogously, though some care must be taken in defining the directions of the various normals and tangents when summing such integrals.

We take $\Gamma = \Gamma(s)$, where s is an arc-length parametrization, to be a smooth curve which lies on the exterior surface $X(\alpha, \beta, t)$ near $X(0, 0, t)$, with preimage $\Gamma_{\alpha\beta}$, so that $\Gamma_{\alpha\beta} \xrightarrow{X(\alpha, \beta, t)} \Gamma$. We require Γ to be pinned at either end at distance $\frac{1}{2}h_\alpha$, $\frac{1}{2}h_\beta$, respectively, from the corner in its preimage. Hence

$$(3.56) \qquad \Gamma(0) = X\left(\frac{h_\alpha}{2}, 0, t\right), \quad \Gamma(L_\Gamma) = X\left(0, \frac{h_\beta}{2}, t\right),$$

where L_Γ denotes the length of Γ. Moreover Γ is taken to orthogonally intersect the bounding plane or thermal groove which lies at each end. For fixed t, let $\Gamma_{\alpha\beta}$ be described in terms of polar coordinates, see Fig. 3, so that

$$(3.57) \qquad \Gamma_{\alpha\beta}(\theta) = \Big(\alpha(\theta), \beta(\theta)\Big) = \Big(r(\theta)\cos\theta, r(\theta)\sin\theta\Big), \quad \theta \in \left[0, \frac{\pi}{2}\right].$$

Then from (3.56)–(3.57), $(\alpha(0), \beta(0)) = (r(0), 0)$, $\left(\alpha\left(\frac{\pi}{2}\right), \beta\left(\frac{\pi}{2}\right)\right) = \left(0, r\left(\frac{\pi}{2}\right)\right)$, and

$$(3.58) \qquad r(0) = \frac{h_\alpha}{2}, \quad r\left(\frac{\pi}{2}\right) = \frac{h_\beta}{2}.$$

From (3.57), we get that $(\alpha_\theta(0), \beta_\theta(0)) = (r_\theta(0), r(0))$, $\left(\alpha_\theta\left(\frac{\pi}{2}\right), \beta_\theta\left(\frac{\pi}{2}\right)\right) = \left(-r\left(\frac{\pi}{2}\right), r_\theta\left(\frac{\pi}{2}\right)\right)$. Though it is a bit technical, the perpendicular intersection requirement implies that

$$(3.59) \qquad r_\theta(0) = -r(0)\frac{\mathbb{F}\left(\frac{h_\alpha}{2}, 0\right)}{\mathbb{E}\left(\frac{h_\alpha}{2}, 0\right)}, \quad r_\theta\left(\frac{\pi}{2}\right) = r\left(\frac{\pi}{2}\right)\frac{\mathbb{F}\left(0, \frac{h_\beta}{2}\right)}{\mathbb{G}\left(0, \frac{h_\beta}{2}\right)},$$

where $\mathbb{E} = \langle X_\alpha, X_\alpha \rangle$, $\mathbb{F} = \langle X_\alpha, X_\beta \rangle$, $\mathbb{G} = \langle X_\beta, X_\beta \rangle$. To be explicit, we take $r(\theta)$ to be Hermit polynomial interpolant of the data $(0, r(0))$, $(0, r_\theta(0))$, $\left(0, r\left(\frac{\pi}{2}\right)\right)$, $\left(0, r_\theta\left(\frac{\pi}{2}\right)\right)$,

namely that $r(\theta) = a + b\,\theta + c\,\theta^2 + d\,\theta^2\left(\theta - \frac{\pi}{2}\right)$, where $a = \frac{h_\alpha}{2}$, $b = -\frac{h_\alpha}{2}\frac{\mathbb{F}\left(\frac{h_\alpha}{2},0\right)}{\mathbb{E}\left(\frac{h_\alpha}{2},0\right)}$, $c =$
$\frac{2}{\pi^2}\left[h_\beta - h_\alpha\left(1 - \frac{\pi}{2}\frac{\mathbb{F}\left(\frac{h_\alpha}{2},0\right)}{\mathbb{E}\left(\frac{h_\alpha}{2},0\right)}\right)\right]$, $d = \frac{2}{\pi^2}\left[h_\beta\left(\frac{\mathbb{F}\left(0,\frac{h_\beta}{2}\right)}{\mathbb{G}\left(0,\frac{h_\beta}{2}\right)} - \frac{4}{\pi}\right) - h_\alpha\left(\frac{\mathbb{F}\left(\frac{h_\alpha}{2},0\right)}{\mathbb{E}\left(\frac{h_\alpha}{2},0\right)} - \frac{4}{\pi}\right)\right]$.

Based on the above prescription, we get if $\nabla_s H = O(1)$ that by the trapezoidal rule

(3.60)
$$\int_\Gamma \overrightarrow{n}^\Gamma \cdot \nabla_s H \, ds = \left(\overrightarrow{n}^\Gamma \cdot \nabla_s H\big|_{s=0} + \overrightarrow{n}^\Gamma \cdot \nabla_s H\big|_{s=L_\Gamma}\right)\frac{L_\Gamma}{2} + O(L_\Gamma^3) =$$
$$= \left(\frac{X_\alpha}{\|X_\alpha\|} \cdot \nabla_s H\bigg|_{\left(\frac{h_\alpha}{2},0\right)} + \frac{X_\beta}{\|X_\beta\|} \cdot \nabla_s H\bigg|_{\left(0,\frac{h_\beta}{2}\right)}\right)\frac{L_\Gamma}{2} + O(L_\Gamma^3),$$

By [18], $L_\Gamma = \int_0^{\frac{\pi}{2}}\sqrt{\mathbb{E}\,r_\theta^2 + 2\,\mathbb{F}\,r_\theta\,r + \mathbb{G}\,r^2}\,\theta$, and again by the trapezoidal rule,

(3.61)
$$L_\Gamma \approx \frac{\pi}{4}\left(\sqrt{\mathbb{E}\,r_\theta^2 + 2\,\mathbb{F}\,r_\theta\,r + \mathbb{G}\,r^2}\bigg|_{\theta=0} + \sqrt{\mathbb{E}\,r_\theta^2 + 2\,\mathbb{F}\,r_\theta\,r + \mathbb{G}\,r^2}\bigg|_{\theta=\frac{\pi}{2}}\right) =$$
$$= \frac{\pi}{6}\left(h_\alpha\,\sqrt{\frac{\mathbb{E}\,\mathbb{G} - \mathbb{F}^2}{\mathbb{E}}}\bigg|_{\left(\frac{h_\alpha}{2},0\right)} + h_\beta\,\sqrt{\frac{\mathbb{E}\,\mathbb{G} - \mathbb{F}^2}{\mathbb{G}}}\bigg|_{\left(0,\frac{h_\beta}{2}\right)}\right).$$

From the definition of $r(\theta)$ and assuming that $\frac{\mathbb{F}\left(\frac{h_\alpha}{2},0,t\right)}{\mathbb{E}\left(\frac{h_\alpha}{2},0,t\right)}$, $\frac{\mathbb{F}\left(0,\frac{h_\beta}{2},t\right)}{\mathbb{G}\left(0,\frac{h_\beta}{2},t\right)}$ are bounded, we may conclude that $r(\theta) = O(\max(h_\alpha, h_\beta))$. Assuming moreover that $\frac{r_\theta}{r}$, $\mathbb{E}$, $\mathbb{F}$, $\mathbb{G}$, are bounded for all $\theta \in \left[0, \frac{\pi}{2}\right]$, we get that $L_\Gamma = O(\max(h_\alpha, h_\beta))$ and that the approximations appearing in (3.60)–(3.61) are $O\left([\max(h_\alpha, h_\beta)]^3\right)$. While the algorithm was implemented in accordance with the discussion above, by applying the trapezoid rule once directly to (3.55), we could have mildly improved the approximation.

3.7. **The governing equations.** Combining the equations and conditions outlined in Sections 3.1–3.6, we obtain the following problem formulation for the evolving equi-spaced parametric surfaces

(3.62)
$$\begin{cases}
\left.\begin{aligned}
\langle X_t^p, \overrightarrow{n}^p\rangle &= \triangle_s H^p \\
\langle X_\alpha^p, X_{\alpha\alpha}^p\rangle = \left\langle X_\beta^p, X_{\beta\beta}^p\right\rangle &= 0
\end{aligned}\right\}, & p \in \Psi_{ext} = \{1,2,3\} \\[2em]
\left.\begin{aligned}
\langle X_t^q, \overrightarrow{n}^q\rangle &= H^q \\
\langle X_\alpha^q, X_{\alpha\alpha}^q\rangle = \left\langle X_\beta^q, X_{\beta\beta}^q\right\rangle &= 0
\end{aligned}\right\}, & q \in \Psi_{gb} := \{4,5,6\} \\[2em]
\text{Boundary Conditions} \\
\text{Initial Conditions}
\end{cases}$$

where for H^p for $p \in \Psi_{ext}$,

$$H = \frac{1}{2} \left\langle \frac{\left\langle X_\beta^p, X_\beta^p \right\rangle X_{\alpha\alpha}^p - 2 \left\langle X_\alpha^p, X_\beta^p \right\rangle X_{\alpha\beta}^p + \left\langle X_\alpha^p, X_\alpha^p \right\rangle X_{\beta\beta}^p}{\left\langle X_\alpha^p, X_\alpha^p \right\rangle \left\langle X_\beta^p, X_\beta^p \right\rangle - \left\langle X_\alpha^p, X_\beta^p \right\rangle^2}, \overrightarrow{n}^p \right\rangle$$

and H^q is similarly defined for $q \in \Psi_{gb}$. In our simulations, the initial conditions were chosen in accordance with Fig. 2.

4. Numerical algorithm

In this section, we present our numerical algorithm for solving the problem formulated in (3.62). The algorithm uses staggered grids and finite difference approximations, which reduce the system to a DAE (differential and algebraic equation) system in time, which is then solved implicitly using Newton iterations.

4.1. **The staggered grids.** Let $X : [0,1]^2 \times [0,T] \to R^2$ represent one of the evolving surfaces, $X^i = X^i(\alpha, \beta, t)$, $i \in \{1, \ldots, 6\}$. Each surface X is spatially approximated on a staggered grid, containing "interior points," "ghost points," and "groove points," see Fig. 4. Let $X_{i,j}^k = X(\alpha_i, \beta_j, t_k)$ denote the approximation of X at staggered grid point (i,j) at time $t_k \in [0,T]$, where $\alpha_i = (i - 1/2) h_\alpha$, $\beta_j = (j - 1/2) h_\beta$, $i \in \{0, \frac{1}{2}, 1, \ldots, N, N + \frac{1}{2}, N + 1\}$, $j \in \{0, \frac{1}{2}, 1, \ldots, M, M + \frac{1}{2}, M + 1\}$, where $h_\alpha = N^{-1}$, $h_\beta = M^{-1}$ reflect the respective interior grid spacings. The indices $(i,j) \in \{1, N\} \times \{1, \ldots, M\}$ refer to interior points, and
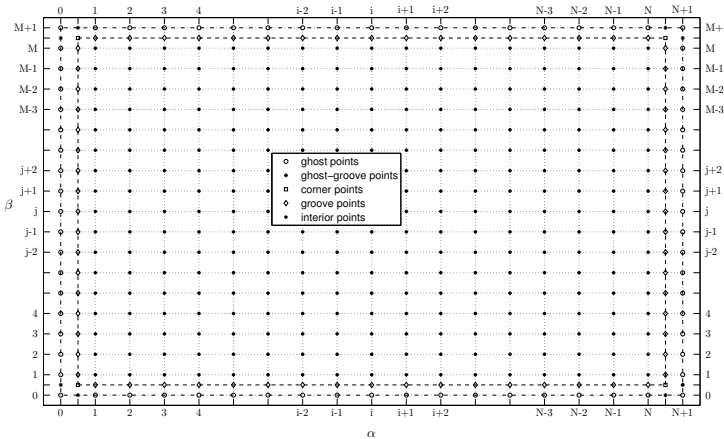

FIGURE 4. The staggered grid mesh. The interior points ($\bullet$) and ghost points($\circ$) are indicated. The groove points are indicted ($\diamond,\square,*$), and the corner points ($\square$) and ghost-groove points ($*$) are marked.

the indices $(i,j) \in \{0, N+1\} \times \{0, 1, \ldots, M, M+1\} \cup \{0, 1, \ldots, N, N+1\} \times \{0, M+1\}$ refer to ghost points. The indices with $(i,j) \in \{\frac{1}{2}, N + \frac{1}{2}\} \times \{0, \frac{1}{2}, \ldots, M, M + \frac{1}{2}, M+1\} \cup (i,j) \in \{\frac{1}{2}, N + \frac{1}{2}\} \times \{0, \frac{1}{2}, 1, \ldots, M, M + \frac{1}{2}, M+1\}$ refer to groove points. Within the set of groove points, we refer to $(i,j) \in \{\frac{1}{2}, N + \frac{1}{2}\} \times \{\frac{1}{2}, M + \frac{1}{2}\}$ as "corner points," and we refer to

$(i,j) \in \{\frac{1}{2}, N+\frac{1}{2}\} \times \{0, M\} \cup \{0, N\} \times \{\frac{1}{2}, M+\frac{1}{2}\}$ "ghost-groove points." The physical boundaries of X, which correspond either to triple junction lines or to free boundary lines, are approximated using the groove points. This approach allows us to use centered finite differences at the interior points as well as at the groove points.

At each time step t^k, the variables $X_{i,j}^k$ at the interior and ghost points are updated, as are $H_{i,j}^k$ for $k \in \Psi_{ext}$, the mean curvatures on the exterior surfaces.

4.2. Approximation of derivatives. Let $\left(\frac{\partial X}{\partial t}\right)_{i,j}^k$ denote the standard forward approximation of X_t at (α_i, β_j, t_k) which has $O(\triangle t_k)$ accuracy with $\triangle t_k = t_k - t_{k-1}$, let $\left(\frac{\partial X}{\partial \alpha}\right)_{i,j}^k$, $\left(\frac{\partial X}{\partial \beta}\right)_{i,j}^k$, denote the standard centered difference approximations which have $O\left((h_\alpha)^2\right)$ and $O\left((h_\beta)^2\right)$ accuracy, respectively, and let $\left(\frac{\partial^2 X}{\partial \alpha^2}\right)_{i,j}^k$, $\left(\frac{\partial^2 X}{\partial \beta^2}\right)_{i,j}^k$, denote the standard centered difference approximations of the second order partial derivatives, whose respective accuracy is given by $O\left((h_\alpha)^2\right)$ and $O\left((h_\beta)^2\right)$. Centered difference approximations of the second mixed derivatives, which have $O\left((h_\alpha)^2 + (h_\beta)^2\right)$ accuracy, are indicated by $\left(\frac{\partial^2 X}{\partial \alpha \partial \beta}\right)_{i,j}^k$. Analogous notation is used to indicate the derivatives of H on the exterior surfaces.

4.3. Approximations along the triple junction lines and free boundary lines. Triple junction lines and exterior free boundary lines are approximated along groove points of the grids, see Fig. 4. Suppose $X_{i,j}^k$ is known at the interior and ghost points, and we wish to approximate X at the groove points. Using the neighboring ghost point and three "collinear" interior points (or ghost points), and Taylor expanding

$$(4.1) \qquad X_{i,\frac{1}{2}}^k = \frac{5 X_{i,0}^k + 15 X_{i,1}^k - 5 X_{i,2}^k + X_{i,3}^k}{16} + O\left((h_\beta)^4\right), \quad i \in \{0, 1, \ldots, N, N+1\}.$$

Similarly, X may be estimated at the other groove points which are not corner points. Using the above estimates, X can be estimated at the corner points. For example,

$$(4.2) \quad X_{\frac{1}{2},\frac{1}{2}}^k \approx \frac{5 \left(X_{\frac{1}{2},0}^k + X_{0,\frac{1}{2}}^k\right) + 15 \left(X_{\frac{1}{2},1}^k + X_{1,\frac{1}{2}}^k\right) - 5 \left(X_{\frac{1}{2},2}^k + X_{2,\frac{1}{2}}^k\right) + \left(X_{\frac{1}{2},3}^k + X_{3,\frac{1}{2}}^k\right)}{32},$$

to $O\left((h_\alpha)^4 + (h_\beta)^4\right)$ accuracy. Obtaining order fourth accuracy in (4.1)-(4.2) allows us to maintain overall second order spatial accuracy in approximating the system (3.7).

The derivatives $\frac{\partial X}{\partial \alpha}, \frac{\partial X}{\partial \beta}$ along the groove can be approximated using second order centered difference approximations with functional evaluations at the ghost points,

$$\left(\frac{\partial X}{\partial \alpha}\right)_{i,j}^k = \frac{X_{i+\frac{1}{2},j}^k - X_{i-\frac{1}{2},j}^k}{h_\alpha} + O\left((h_\alpha)^2\right), \quad \left(\frac{\partial X}{\partial \beta}\right)_{i,j}^k = \frac{X_{i,j+\frac{1}{2}}^k - X_{i,j-\frac{1}{2}}^k}{h_\beta} + O\left((h_\beta)^2\right).$$

Similar approximations are used to estimate the mean curvature H and its derivatives along the triple junction lines and external free boundary lines on the exterior surfaces.

4.4. Numerical solution of the DAE system. Let $n \in \mathbb{N}$ and $T > 0$ be given, and let us consider the solution of the following general system of n DAE

$$(4.3) \qquad\qquad \mathbf{F}\left(Y', Y, t\right) = 0, \quad t \in (0, T], \quad Y(0) = Y_0,$$

where $Y(t) = (y_1(t), \ldots y_n(t))$, $Y : [0, T] \to \mathbb{R}^n$, and $Y_0 \in \mathbb{R}^n$ is prescribed. Let $Y^k = Y(t^k)$ denote an approximation of Y at time $0 \leq t_k \in [0, T]$, for $k = 0, 1, \ldots, N_{T_{max}}$, $N_{T_{max}} \in \mathbb{N}$, with $t_0 = 0$, and set $\triangle t_k = t_k - t_{k-1}$. Applying the backward Euler method [2] to the system given in (4.3), we obtain the following $n \times n$ system of nonlinear equations for Y^k,

$$(4.4) \qquad\qquad \mathbf{F}\left(\frac{Y^k - Y^{k-1}}{\triangle t_k}, Y^k, t_k\right) = 0, \ k = 1, \ldots, N_{T_{max}}, \quad Y^0 = Y_0.$$

Noting that $\mathbf{F} : \mathbb{R}^n \to \mathbb{R}^n$ has n components, $f_i = f_i\left(\frac{Y^k - Y^{k-1}}{\triangle t_k}, Y^k, t_k\right)$, $i = 1, \ldots, n$, its Jacobian with respect to Y^k can be expressed as

$$(4.5) \qquad\qquad \begin{pmatrix} \frac{\partial f_1}{\partial y_1^k} & \cdots & \frac{\partial f_1}{\partial y_n^k} \\ \vdots & \ddots & \vdots \\ \frac{\partial f_n}{\partial y_1^k} & \cdots & \frac{\partial f_n}{\partial y_n^k} \end{pmatrix}.$$

For $k = 1, \ldots, N_{T_{max}}$, we use Newton's iteration method to find successively better approximations to the zeroes (roots) of $F(Y)$ until an estimate of the local error is not greater than some prescribed tolerance, $0 < \widetilde{\varepsilon} \ll 1$. We chose $\widetilde{\varepsilon} = 10^{-11}$ to achieve accuracy comparable to the estimated accuracy in the approximation of the Jacobian matrix. Additionally, we set a tolerance bound of $\widehat{\varepsilon} = 10^{-6}$ on $F(Y)$. See Algorithm 1 in Appendix.

4.5. Approximation of the Jacobian matrix. We approximate the Jacobian matrix (4.5) numerically, based on the central difference approximations

$$(4.6) \qquad\qquad \frac{\partial F_i}{\partial y_j} = \frac{F_i\left(y + \varepsilon\, e_j\right) - F_i\left(y - \epsilon\, e_j\right)}{2\,\epsilon} + O\!\left(\varepsilon^2\right),$$

where $e_j = (0, \ldots, \overbrace{1}^{\text{element } j}, \ldots, 0)$ and ε is a small positive parameter. In [35] the suggestion is made to chose $\varepsilon = \epsilon_M^{1/3}$, where ϵ_M is the machine epsilon. Adopting this approach in our double precision setting yields $\epsilon_M^{2/3} \approx 10^{-11}$ accuracy in (4.6). See Algorithm 2 in Appendix.

4.6. A numerical algorithm. We outline below our numerical algorithm for solving the system (3.62). We consider H^p, the mean curvature of the exterior surfaces S^p, $p \in \Psi_{ext}$ as additional variables. Accordingly we do not need to calculate the third and fourth derivatives of X with respect to α, β. We discretize each exterior surface using staggered grids, as indicated above, with $N \times N$ interior grid points. Similarly we discretize each grain boundary surface using staggered grids with $N \times M$ interior grid points.

We choose initial conditions in accordance with the configuration portrayed in Fig. 2. At time t_k, let $(X_{i,j}^k)^p$ and $(H_{i,j}^k)^p$, $p \in \Psi_{ext}$, denote the value of X^p and H^p at grid point (i, j), and let $(X_{i,j}^k)^q$, $q \in \Psi_{gb}$, denote the value of X^q at grid point (i, j). Discretization of the governing equations requires approximation of the time derivatives of X^p, X^q, as well as of the first and second derivatives of X^p, H^p and X^q with respect to α and β at the interior grid points. Discretization of the boundary conditions requires approximations for X^p, H^p

and X^q and their first derivatives with respect to α and β along the groove points of the grid.

The discretization of the governing equations and boundary conditions yields an ODAE system, which we indicate for simplicity by

$$(4.7) \qquad\qquad F\left(U', U, t\right) = 0, \quad t \in (0, T], \quad U(0) = U_0.$$

In (4.7), $U = (u_1, u_2, \ldots, u_\ell, \ldots)$ is taken to reflect a fairly natural ordering of the elements

$$(X_{i,j})^p = \left((x_{i,j})^q, (y_{i,j})^q, (z_{i,j})^q \right), (H_{i,j}^k)^p, \quad (X_{i,j})^q = \left((x_{i,j})^q, (y_{i,j})^q, (z_{i,j})^q \right),$$

which are defined at the interior and ghost points of the various grids used in approximating S^p and S^q respectively. The vector U contains $3\,(N+2)\,(4\,N+M+14)$ elements and does not include evaluations along the groove points, since the variables and equations at the groove points are prescribed with the help of the interior and ghost points using (4.1)-(4.2).

We solve (4.7) in accordance with the discussion in Sections 4.4 and 4.5. See Algorithms 1 and 2 in the Appendix. The overall accuracy of our discretization is $O\left((h_\alpha)^2 + (h_\beta)^2\right)$ in space and $O(\triangle t)$ in time. Although we do not prove convergence, we tested for self-consistency of our method by taking smaller time steps and grid partitions.

By considering the governing equations and boundary conditions, it can be seen that changes in the entries at some grid point (i, j) influence the values of the entries only in some small neighborhood of grid points around the grid point. By defining a neighborhood for each grid point and undertaking functional evaluations only in this neighborhood, the running time for the algorithm could be reduced by partial parallelization.
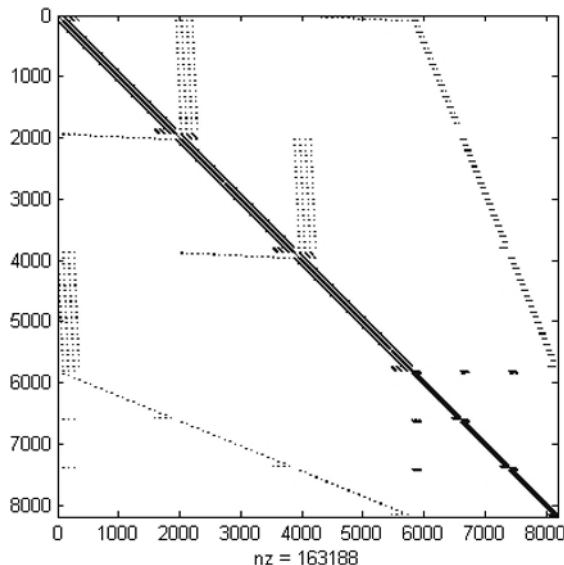

FIGURE 5. Visualization of the $nz = 163188$ nonzero entries in the Jacobian matrix for our system where $m = 0.1$, $Lx = 30$, $Ly = 30$, $Lz = 0.25$, with $\triangle t = 0.25$, $N = 20$, $M = 10$.

The resultant Jacobian matrix, which we denote as A, is sparse and not symmetric, see Fig 5. We used the MATLAB UMFPACK [12] solver for solving $A\,x = b$. With regard to software, the algorithm was implemented in "C", together with various extension and packages, and the postprocessing was undertaken in MATLAB. The calculations of the function F and its Jacobian J were done in parallel using the MPI or "Message Passing Interface" [30] library of extensions to "C". The simulations were run on the RBNI high-performance "NANCO" computer of Technion Center for Computational Nanoscience and Nanotechnology.

5. Numerical results and tests

5.1. **Some numerical results.** Simulations were undertaken for the initial conditions portrayed in Fig 2, with $L_x = L_y = 30$, $L_z = 0.25$, $m \in \mathcal{M}$, where $\mathcal{M} = \{0.0, 0.001, 0.01, 0.05, 0.01\}$, for $0 \le t \le 100$ with $N = 50$, $M = 25$, $\triangle t = 0.5$. Note that the values $L_x = L_y = 30$, $L_z = 0.25$ are appropriate for modeling thin films, since the height to width ratio is $L_z/L_x = L_z/L_y = 1/120$. We also tested our program with other values of L_x, L_y, L_z, such as $L_x = L_y = L_z = 1$, and with other values for N, M, $\triangle t$.

Results from a numerical simulation with $m = 0.1$ and $L_x = L_y = 30$, $L_z = 0.25$ can be seen in Fig. 6. As expected, formation of thermal grooves can be observed. It is not clear whether annihilation of the corner grain will eventually occur here prior to break up of the thin film. Considerable pitting seems to be occurring at the quadruple point as well as at the corner point, II^t, which is located above $(x, y) = (0, 0)$.

In Fig. 7, the heights at the quadruple junction and at corner points from simulations with $m \in \mathcal{M}$ where $\mathcal{M} = \{0.0, 0.001, 0.01, 0.05, 0.01\}$, and $L_x = L_y = 30$, $L_z = 0.25$, can be seen. Due to symmetry, the behavior at the corner points IV^t, C^{II}, is the same as at III^t, C^I, respectively, and has not been portrayed. Note the monotone decrease in the height at the quadruple point and at the corner points II^t, IV^t, whereas the behavior of the height at the corner points C^I, C^{III} is nonmonotone.

5.2. **Comparison with the von Neumann-Mullins law.** Von Neumann and Mullins developed a formula [32, 51] for the evolution of the surface area, $\mathcal{S}(t)$, of a grain, which is embedded in R^2 with n trijunctions along its perimeter, within a planar network of grains with grain boundaries that evolve by mean curvature motion, $V_n = A\kappa$, namely,

$$(5.1) \qquad \frac{d\mathcal{S}}{dt} = \frac{A\pi}{3}(n - 6).$$

The "corner grain" in our system, whose exterior surface, S^3, contains the corner point C^{III}, may be viewed, by extending our three grain system by mirror symmetry, as one quarter of an embedded grain with four trijunctions along its perimeter.

In our system, when $m = 0$ the exterior surfaces remain flat and the grain boundaries evolve by mean curvature motion, $V_n = \mathcal{A}H$, where H is the average of the principle curvatures, see (2.1),(3.4); under these circumstances, writing (5.1) in terms of our dimensionless variables, we find for the surface area of the corner grain, $|S^3|$, that

$$(5.2) \qquad \frac{d|S^3|}{dt} = -\mathcal{A}\pi/12.$$

Integrating (5.2) yields that $|S^3|(t) = |S^3|(0) - \pi\,t/12$, which implies that the corner grain should annihilate at time $T_a = 12|S^3|(0)/\pi$. If $0 < m \ll 1$ and if the specimen is sufficiently
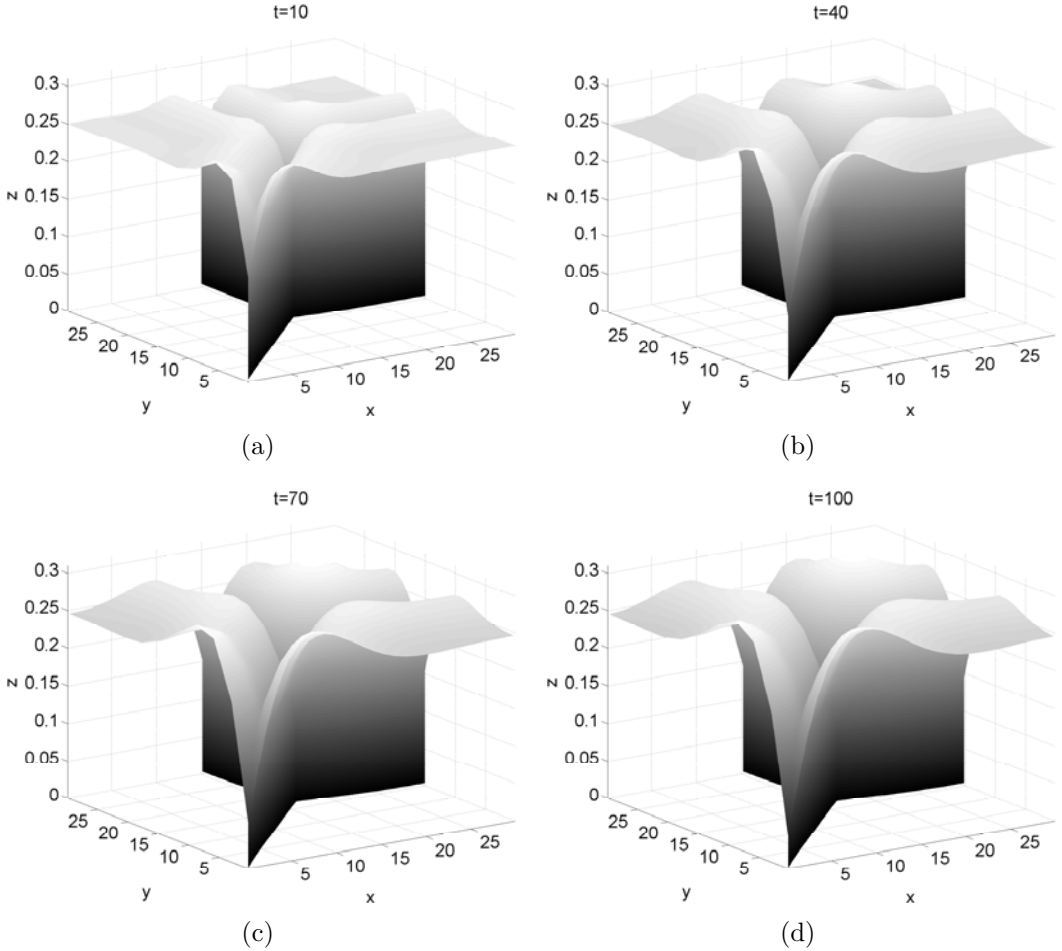
FIGURE 6. Simulation results for $m = 0.1$, $L_x = L_y = 30$, $L_z = 0.25$, at times (a) $t = 10$, (b) $t = 40$, (c) $t = 70$, (d) $t = 100$. Pitting can be seen at the quadruple junction as well as at the corner point, II^t.

thick, then (5.2) should still be roughly accurate. However break up may occur before the grain annihilates if the specimen is too thin, and (5.2), as an approximation, becomes inaccurate as m is increased.

In Fig. 8, the area of S^3 is portrayed for $m \in \mathcal{M}$, where $\mathcal{M} = \{0.0, 0.001, 0.01, 0.05, 0.01\}$, as a function of time. When $m = 0.0$, the surface area evolves in accordance with (5.2), and decreases linearly. Monotone decrease is seen for all values of $m \in \mathcal{M}$; however, as m increases, the decrease rate slows, implying that grain annihilation should take longer. This corroborates the predictions in [26] that for relatively small thin specimens, groove formation should slow grain boundary migration. It follows from the formula $T_a = 12|S^3|(0)/\pi$ that when $m = 0$, annihilation of the corner grain in our simulation should occur at time $T_a \approx 859.4$, and the results portrayed in Fig. 8 indicate that $T_a > 859.4$ when $m > 0$. Since the
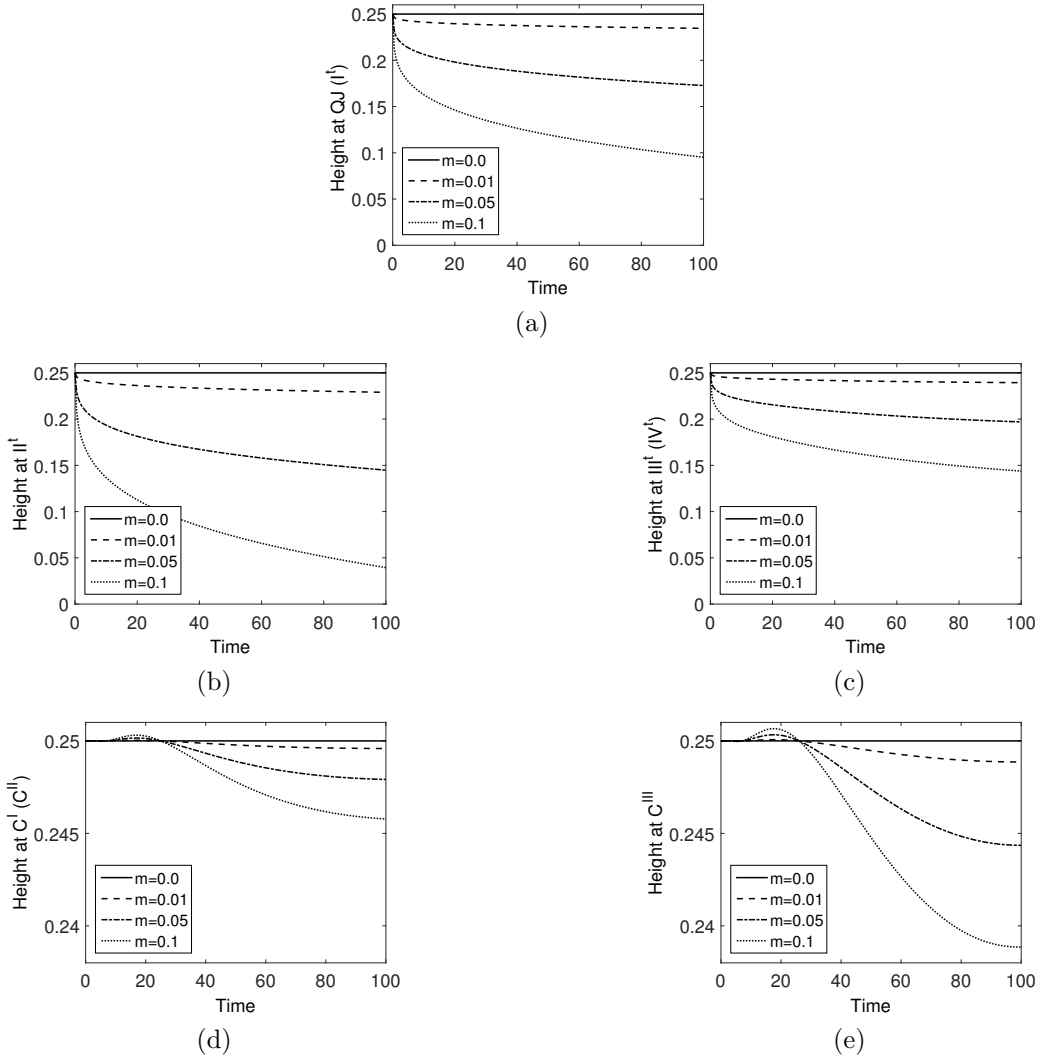
FIGURE 7. The heights at (a) the quadruple junction, at the corner points (b) II^t, (c) III^t, and at the corner points (d) C^I, (e) C^{III}, as functions of time for $m \in \mathcal{M}$ where $\mathcal{M} = \{0.0, 0.001, 0.01, 0.05, 0.01\}$. Here $L_x = L_y = 30$, $L_z = 0.25$. In accordance with Fig. 6, the height at the quadruple junction and at II^t, III^t exhibit monotone decrease, whereas the heights at C^I, C^{III} appears to oscillate.

simulations reflected in Fig. 6 were undertaken for $m = 0.1$ with $0 \le t \le 100$, it is not surprising that annihilation was not seen.
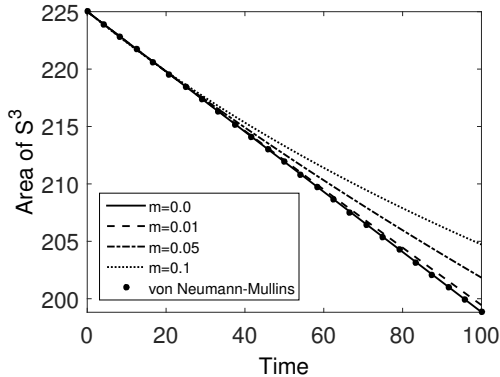
FIGURE 8. Comparison with the von Neumann-Mullins law. For $m \in \mathcal{M}$ where $\mathcal{M} = \{0.0, 0.001, 0.01, 0.05, 0.01\}$, the area of S^3, $|S^3|$, decreases monotonically. When $m = 0.0$, the area of S^3 decreases linearly in accordance with the von Neumann-Mullins law. Here surface diffusion appears to slow the rate at which the smallest grain shrinks.

5.3. **Verifying mass conservation and energy dissipation.** Assuming sufficient regularity, our problem formulation can be shown to satisfy [14, 36]

$$(5.3) \qquad \sum_{i \in \Psi_{ext}} \int_{S^i} V_n \, dS = 0,$$

where $\int_{S^i} V_n \, dS$ is the integral of the normal velocity over the surface S^i, which implies conservation of the total volume of our three grain system. Assuming that the density of our 3 grain system, composed of 3 grains of the same (isotropic) material, is constant, (5.3) also implies mass conservation.

Our problem formulation can also be shown to satisfy [14, 36]

$$(5.4) \quad \frac{d}{dt}\left\{ \sum_{i \in \Psi_{ext}} |S^i| + m \sum_{i \in \Psi_{gb}} |S^i| \right\} = -\mathcal{B} \sum_{i \in \Psi_{ext}} \int_{S^i} |\nabla_s H^i|^2 \, dS - m\mathcal{A} \sum_{i \in \Psi_{gb}} \int |H^i|^2 \, dS.$$

where $|S^i|$ is the surface area of surface S^i. Equation (5.4) is an energy dissipation equality, prescribing the rate of dissipation of the (dimensionless) total energy in the system,

$$E_{system} := \left\{ \sum_{i \in \Psi_{ext}} |S^i| + m \sum_{i \in \Psi_{gb}} |S^i| \right\} = \frac{1}{\gamma_{ext}} \left\{ \gamma_{ext} \sum_{i \in \Psi_{ext}} |S^i| + \gamma_{gb} \sum_{i \in \Psi_{gb}} |S^i| \right\},$$

where γ_{ext} and γ_{gb} are the surface free energies of the exterior surfaces and the grain boundaries, respectively, and $m = \gamma_{gb}/\gamma_{ext}$.

In Fig. 9a, mass conservation of our algorithm is verified in that the relative variation in the total volume of the system, $[V(t) - V(0)]/V(0)$ is $\approx 10^{-4}$, in accordance with the accuracy of our numerical scheme. In Fig. 9b, we see that E_{system} decreases in accordance with (5.4) after a short initial transient. The initial transient is apparently due to the lack of compatibility of the initial conditions with the boundary conditions (Young's law) along the thermal grooves.
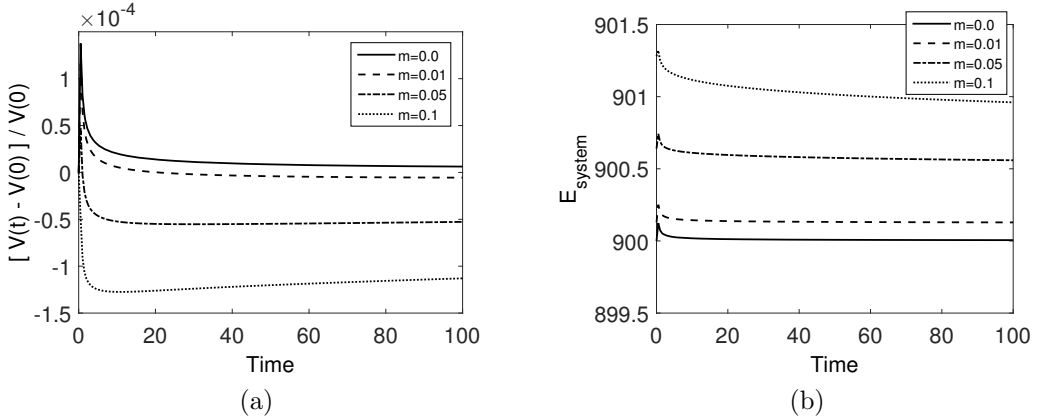
FIGURE 9. For $L_x = L_y = 30$, $L_z = 0.25$, $m \in \mathcal{M}$, where $\mathcal{M} = \{0.0, 0.001, 0.01, 0.05, 0.01\}$, (a) the relative total volume of the system, $[V(t) - V(0)]/V(0)$, and (b) the (dimensionless) weighted surface area, E_{system}, as functions of time, see (5.3)–(5.4). Note that $|V(t) - V(0)|/|V(0)| < 10^{-4}$, and E_{system} exhibits monotone decrease following a short initial transient. After the initial transient, the variation in $|V(t) - V(0)|/|V(0)|$ is also smaller.

5.4. **Comparison with Mullins (1957) and Génin, Mullins, Wynblatt (1992).** Mullins (1957) [33] and Génin, Mullins & Wynblatt (1992) [22] studied grooving and pitting phenomena based on a small slope linearized approximation of surface diffusion, which is valid in the limit $m \to 0$. More specifically, Mullins [33] considered the thermal groove resulting from an initially flat grain boundary which perpendicularly intersected an initially flat exterior surface of infinite extent. Based on the small slope approximation, he estimated the height of the thermal groove to be given by

(5.5)
$$h_M(t) = h_0 - \frac{m}{2^{3/4}\,\Gamma(5/4)\,\sqrt{4-m^2}}\,t^{1/4}.$$

where $\Gamma(\cdot)$ is the Gamma function. Génin, Mullins & Wynblatt [22] considered the pitting which occurs where two thermal grooves develop on an initially flat exterior surface of infinite extent, which is bounded by two planar grain boundaries which are constrained to remain planar, to perpendicularly intersect the exterior surface, and to intersect each other at a prescribed angle ψ. Based on the small slope approximation, they numerically showed the height at the point of intersection to be given by

(5.6)
$$h_{GMW}(t,\,\psi) = h_0 - \frac{m\,f(\psi)}{2^{3/4}\,\Gamma(5/4)\,\sqrt{4-m^2}}\,t^{1/4}.$$

where $\Gamma(\cdot)$ is the Gamma function and $f(\psi)$ is a monotonically decreasing function of the angle ψ. They estimated $f(\psi)$ for various values of ψ, and found that $f(72°) \approx 2.5$, $f(108°) \approx 1.66$, $f(126°) \approx 1.4$. Moreover they demonstrated analytically that $f(90°) = 2$, and it follows from (5.5) that $f(180°) = 1$. Using cubic spline interpolation based on their data, we estimated that $f(120°) \approx 1.479$.
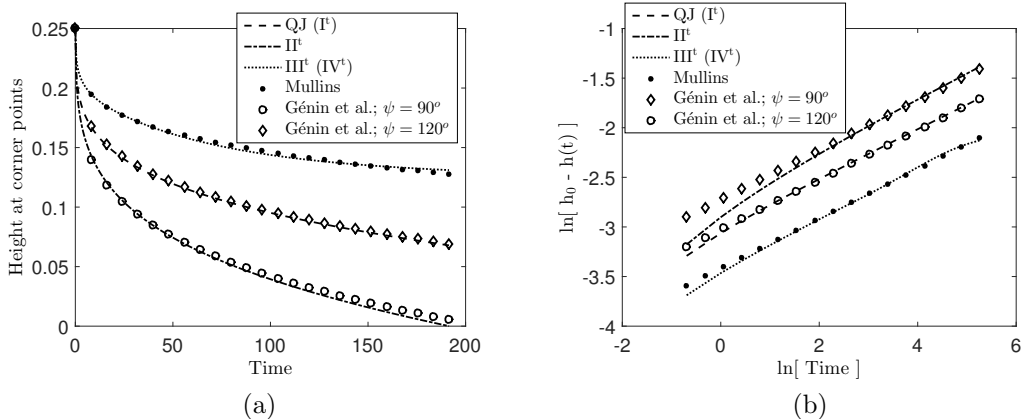
FIGURE 10. From simulations with $m = 0.1$. (a) The height at the various corner points, and (b) the natural logarithm of the normalized height at the various corner points, as functions of time.

In Fig. 10a, we compare the evolution of the height at the quadruple junction, QJ, and the height of the various corner points with the predictions of Mullins [33] and Génin, Mullins & Wynblatt [22]. One can clearly see that the height at II^t behaves roughly like $h_{GMW}(t, 90°)$, the height at the quadruple junction QJ behaves roughly like $h_{GMW}(t, 120°)$, and the height at $III^t(IV^t)$ behaves roughly like $h_M(t)$, see (5.5), (5.6). Taking into account the geometry of the system (see Fig. 2), these similarities are to be expected if nonlinear effects and finite system effects can be neglected. In Fig. 10b, we can see that the behavior of the heights of all of the corner points is approximately proportional to $t^{1/4}$; this behavior is reasonable since $m = 0.1$ here, though at later times nonlinear effects and finite system effects should become more apparent.

6. CONCLUSIONS

We have developed a robust algorithm designed to follow the coupled evolution by surface diffusion of the exterior surfaces with internal grain boundary migration by motion by mean curvature in systems containing a small number of grains. Our algorithm has been verified in several ways. We have shown that it conserves mass and dissipates energy to within the accuracy of the algorithm. It reproduces the predictions of the von Neumann-Mullins law [32, 51] in the limit $m \to 0$. Moreover for $0 < m \ll 1$, it reproduces Mullins' [33] classical grooving predictions at the grooves which form along the exterior boundaries of the domain, and at appropriately constrained trijunctions, it reproduces the predictions of Génin, Mullins, Wynblatt [22] for $\psi = 120°$.

The geometry treated in this paper is portrayed in Fig. 11a. Our numerical approach can be readily adapted to treat other geometries, such as the geometries portrayed in Fig. 11. More specifically, the geometries in Figs. 11b, 11c were studied in [7], that in 11d was studied in [14, 15, 17], and the geometries portrayed in Figs. 11e, 11f are reminiscent of geometries discussed in [46]. The geometries in Fig. 11d, 11f are relevant in particular to the study of pitting.
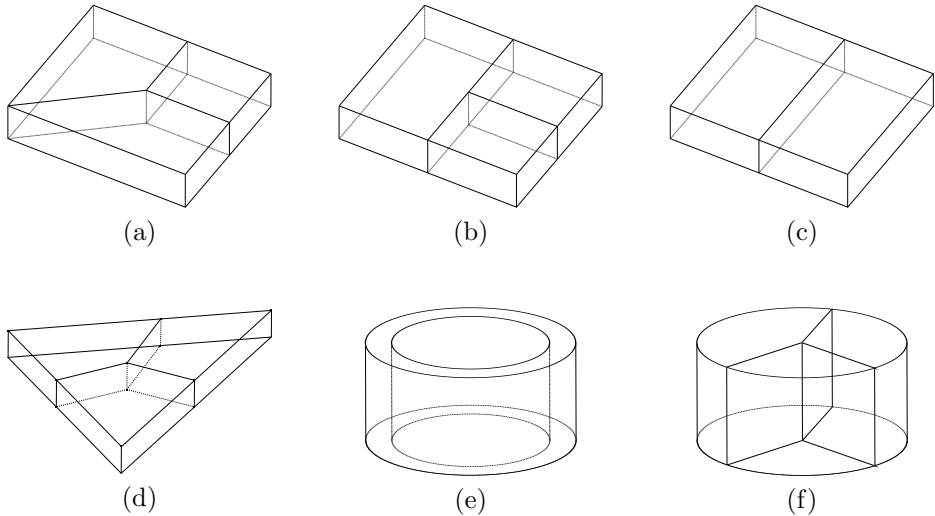
FIGURE 11. Our algorithm can be adapted to follow the evolution of the grain systems portrayed above.

It should be possible to incorporate additional effects, such as elastic stresses or various types of defects, by coupling our system of equations with additional fields. It should be rather straightforward, though a bit technical, to include anisotropy. While these effects may also be incorporated within the framework of finite element methods [8], we emphasize that even within the isotropic framework treated here, it appears that we are the first to be able to undertake realistic 3D simulations of phenomena such as pitting, grain annihilation, hole formation, and more recently dewetting phenomena and stabilization of hexagonal arrays [15, 17, 16].

An eventual goal is to treat many grain systems, starting perhaps by considering nano-crystalline specimens which are several grains deep. In this context it may be possible to use our approach to describe the evolution of the exterior surfaces, coupled with a level set approach to follow the evolution of the grain boundaries within the interior. If, using hybrid methods as suggested above or some other methods, we find new phenomena of interest, we may adjust our algorithm to focus in locally on the details of the dynamics.

Algorithm 1 Calculating an approximate solution to the discretized system

---

Input: U^0, $\tilde{\varepsilon}$, $N_{T_{max}}$, $\{\triangle t_k\}_1^{N_{T_{max}}}$, N_{max}
Output: U^k for $k = 1, ..., N_{T_{max}}$

    Set $\widehat{\varepsilon} = 10^{-6}$
    Set $t = 0$
    for $k = 1, \ldots, N_{T_{max}}$ **do**
        $V = U^{k-1}$
        Set $t = t + \triangle t_k$
        Set $i = 1$
        repeat
            Calculate $F\left(\frac{V - U^{k-1}}{\triangle t_k}, V, t\right)$
            Calculate the Jacobian $J(V)$, see Algorithm 2
            Solve $J(V)\,\delta = -F(V)$ (a linear system, $A\,x = b$)
            Update $V = V + \delta$
            Set $i = i + 1$
        until $||F(V)|| \leq \tilde{\varepsilon}$ **or** $||\delta|| \leq \tilde{\varepsilon}$ **or** $i > N_{max}$
        if $||F(V)|| > \widehat{\varepsilon}$ **then**
            stop the algorithm   ▷ the desired tolerance cannot be achieved
        end if
        Set $U^k = V$
    end for

Algorithm 2 Approximating the Jacobian

Input: V, F, N, M
Output: Jacobian J

    Set $Length = 3\,N\,(4\,N + 3\,M)$
    Set $\varepsilon = 10^{-6}$
    for $i = 1, \ldots, Length$ **do**
    Set $e = (0, \ldots, \overbrace{1}^{\text{element } i}, \ldots, 0)$
    Calculate $F(V + \varepsilon\,e)$
    Calculate $F(V - \varepsilon\,e)$
    Set column i in matrix J to be $\frac{F(V + \varepsilon\,e) - F(V - \varepsilon\,e)}{2\,\varepsilon}$
    end for

REFERENCES

[1] T. Asai and Y. Giga. On self-similar solutions to the surface diffusion flow equations with contact angle boundary conditions. *Interfaces Free Bound.*, 16:539–573, 2014.

[2] U.M. Asher and L.R. Petzold. *Computer Methods for Ordinary Differential Equations and Differential – Algebraic Equations*. SIAM, 1998.

[3] A. Averbuch, M. Israeli, and I. Ravve. Electromigration of intergranular voids in metal films for microelectronic interconnects. *J. Comp. Phys.*, 186:481–502, 2003.

[4] K. Barmak, E. Eggeling, D. Kinderlehrer, R. Sharp, S. Ta'asan, A.D. Rollett, and K.R. Coffey. Grain growth and the puzzle of its stagnation in thin films: the curious tale of a tail and an ear. *Prog. Mat. Sci.*, 58:987–1055, 2013.

[5] K. Barmak, M. Emelianenko, D. Golovaty, D. Kinderlehrer, and S. Ta'asan. Towards a statistical theory of texture evolution in polycrystals. *SIAM J. Sci. Comput.*, 30:3150–3169, 2008.

[6] J.W. Barrett, H. Garcke, and R. Nürnberg. On the variational approximation of combined second and fourth order geometric evolution equations. *SIAM J. Scient. Computing*, 29:1006–1041, 2007.

[7] J.W. Barrett, H. Garcke, and R. Nürnberg. Finite element approximation of coupled surface and grain boundary motion with applications to thermal grooving and sintering. *Euro. J. Appl. Math.*, 21:519–556, 2010.

[8] J.W. Barrett, H. Garcke, and R. Nürnberg. Parametric approximation of surface clusters driven by isotropic and anisotropic surface energies. *Interfaces Free Boundaries*, 12:187–234, 2010.

[9] J.W. Barrett, H. Garcke, and R. Nürnberg. The approximation of planar curve evolutions by stable fully implicit finite element schemes that equidistribute. *Numer. Methods Partial Diff. Eqs.*, 27:1–30, 2011.

[10] M. Beck, Z. Pan, and B. Wetton. Stability of travelling wave solutions for coupled surface and grain boundary motion. *Physica D*, 239:1730–1740, 2010.

[11] R. Carel, C.V. Thompson, and H.J. Frost. Computer simulation of strian energy effects vs surface and interface energy effects on grain growth in thin films. *Acta Mater.*, 44:2479–2494, 1996.

[12] T.A. Davis. *UMFPACK User Guide, Version 5.4.0.* Univ. of Florida, Gainesville, FL, May 20, 2009. http://www.cise.ufl.edu/research/sparse/umfpack/.

[13] V. Derkach. *Surface evolution and grain boundary migration in a system of 5 grains.* M.Sc. Thesis, Department of Mathematics, Technion–IIT, Israel, 2010.

[14] V. Derkach. *Surface and Grain Boundary Evolution in Thin Single- and Poly-crystalline Films.* PhD. Thesis, Department of Mathematics, Technion–IIT, Israel, submitted 2016.

[15] V. Derkach, A.Novick-Cohen, A. Vilenkin, and E. Rabkin. Grain boundary migration and grooving in thin 3-D systems. *Acta Mater.*, 65:194–206, 2014.

[16] V. Derkach, A. Novick-Cohen, and E. Rabkin. Grain boundaries effects on hole morphology and growth during solid state dewetting of thin films. in preparation.

[17] V. Derkach, A. Novick-Cohen, and A. Vilenkin. Geometric interfacial motion: Coupling surface diffusion and mean curvature motion. In *Submitted to Proceedings of the MNP2015, Springer, in honor of Y.Giga's 60th birthday*, Hokkaido, 2015.

[18] M.P. do Carmo. *Differential Geometry of Curves and Surfaces.* Prentice–Hall, 1976.

[19] S. Esedoglu, S. Ruuth, and R. Tsai. Threshold dynamics for high order geometric motions. *Interfaces Free Boundaries*, 10:263–282, 2008.

[20] S. Gallot, D. Hulin, and J. Lafontaine. *Riemannian geometry.* Springer, 2004.

[21] H. Garcke and A. Novick-Cohen. A singular limit for a system of degenerate Cahn–Hilliard equations. *Adv. Diff. Eqns.*, 5:401–434, 2000.

[22] F.Y. Génin, W.W. Mullins, and P. Wynblatt. Capillary instabilities in thin films: a model of thermal pitting at grain boundary vertices. *Acta. Metall. Mater.*, 40:3239–3248, 1992.

[23] G. Gottstein and L.S. Shvindlerman. *Grain Boundary Migration in Metals: Thermodynamics, Kinetics, Applications.* 2nd edition, CRC, 2010.

[24] C. Herring. Surface tension as a motivation for sintering. *in: The Physics of Powder Metallurgy*, pages 143–179, 1951. Ed.: W.E.Kingston. McGraw–Hill.

[25] C. Herring. The use of classical macroscopic concepts in surface-energy problems. *in: Structure and Properties of Solid Surfaces*, 1953. Eds.: R.Gomer, C.S.Smith. Chicago.

[26] J. Kanel, A. Novick-Cohen, and A. Vilenkin. A traveling wave solution for coupled surface and grain boundary motion. *Acta. Mater.*, 51:1981–1989, 2003.

[27] J. Kanel, A. Novick-Cohen, and A. Vilenkin. Coupled surface and grain boundary motion: a travelling wave solution. *Nonlinear Analysis TAM*, 59:1267–1292, 2004.

[28] J. Kanel, A. Novick-Cohen, and A. Vilenkin. A numerical study of grain boundary motion in bicrystals. *Acta. Mater.*, 53:227–235, 2005.

[29] B. Merriman, J.K. Bence, and S.J. Osher. Diffusion generated motion by mean curvature. *in: Computational Crystal Growers Workshop*, pages 73–83, 1992. Ed.: J. Taylor, AMS.

[30] Message Passing Interface Forum. *MPI: A Message–Passing Interface Standard, Version 2.2*, September 4, 2009. http://www.mpi–forum.org/.

[31] D. Min and H. Wong. A model of migrating grain-boundary grooves with application to two mobility-measurement methods. *Acta Mater.*, 50:5155–5169, 2002.

[32] W.W. Mullins. Two-dimensional motion of idealized grain boundaries. *J. Appl. Phys.*, 28:900–904, 1956.

[33] W.W. Mullins. Theory of thermal grooving. *J. Appl. Phys.*, 28:333–339, 1957.

[34] W.W. Mullins. The effect of thermal grooving on grain boundary motion. *Acta Metall.*, 6:414–427, 1958.

[35] J. Nocedal and S.J. Wright. *Numerical Optimization*. Springer Science + Business Media, 1999.

[36] A. Novick-Cohen. Order–disorder and phase separation: modeling grain sintering. *in: Continuum models and discrete systems*, pages 56–68, 1998. Istanbul, World Sci.

[37] A. Novick-Cohen. Triple-junction motion for an Allen-Cahn/Cahn-Hilliard system. *Phys. D*, 137:1–24, 2000.

[38] A. Novick-Cohen, O. Zelekman-Smirin, and A. Vilenkin. The effects of grain grooves on grain boundary migration in nanofilms. *Acta Mater.*, 58:813–822, 2010.

[39] Z. Pan. Numerical study for coupled surface and grain boundary motion. PhD. Thesis, Department of Mathematics, UBC, Canada, 2008.

[40] Z. Pan and B. Wetton. A numerical method for coupled surface and grain boundary motion. *Eur. J. Appl. Math.*, 19:311–327, 2008.

[41] Z. Pan and B. Wetton. Numerical simulation and linear well-posedness analysis for a class of three-phase boundary motion problems. *J. Comput. Appl. Math.*, 236:3160–3173, 2012.

[42] E. Rabkin, L. Klinger, and V. Semenov. Grain boundary grooving at the singular surfaces. *Acta Mater.*, 48:1533–1540, 2000.

[43] T. Radetic, C. Ophus, D.L. Olmsted, M. Asta, and U. Dahmen. Mechanism and dynamics of shrinking island grains in mazed bicrystal thin films of AU. *Acta Mater.*, 60:7051–7063, 2012.

[44] G.S. Rohrer. Measuring and interpreting the structure of grain boundary networks. *J. Amer. Ceramic Soc.*, 94:633–646, 2011.

[45] K.A. Smith, F.J. Solis, and D.L. Chopp. A projection method for motion of triple junctions by level sets. *Interfaces Free Boundaries*, 4:263–276, 2002.

[46] D.J. Srolovitz and S.A. Safran. Capillary instabilities in thin films. I. Energetics. *J. Appl. Phys.*, 60:247–254, 1986.

[47] B. Sun, Z. Suo, and W. Yang. A finite element method for simulating interface motion–I. migration of phase and grain boundaries. *Acta Mat.*, 45:1907–1915, 1997.

[48] C.V. Thompson. Solid state dewetting of thin films. *Ann. Rev. Mater. Res.*, 42:399–434, 2012.

[49] C.E. Torres, M. Emelianenko, D. Golovaty, D. Kinderlehrer, and S. Ta'asan. Numerical analysis of the vertex models for simulating grain boundary networks. *SIAM J. Appl. Math.*, 75:762–786, 2015.

[50] A. Vilenkin, R. Kris, and A. Brokman. Breakup and grain growth in thin-film array. *J. Appl. Phys.*, 81:238–245, 1997.

[51] J. von Neumann. Discussion: Grain shapes and other metallurgical applications of topology. *in Metal Interfaces, ed. Herring, C., American Society for Metals, Cleveland, OH*, 56:108–110, 1952.

[52] H. Zhang and H. Wong. Coupled grooving and migration of inclined grain boundaries: regime II. *Acta Mater.*, 50:1995–2012, 2002.

Department of Mathematics, Technion-IIT, Haifa 32000, Israel
E-mail address: `vadder@tx.technion.ac.il`

Department of Mathematics, Technion-IIT, Haifa 32000, Israel
E-mail address: `amync@tx.technion.ac.il`

Racah Institute of Physics, The Hebrew University, Jerusalem 91904, Israel
E-mail address: `vilenkin@mail.huji.ac.il`